Modelling of Folding Wing-Tip Devices for Gust Loads Alleviation

R.C.M. Cheung[1], C. Wales[2], D. Rezgui[3], J.E. Cooper[4]
University of Bristol, Department of Aerospace Engineering, University Walk, Bristol, BS8 1TH, UK.

and

T. Wilson[5]
Airbus Operations Ltd, Filton, Bristol, BS34 7PA, UK.

High aspect ratio wings have been the focus of recent aircraft designs for improved fuel consumption through reducing induced drag. The increase in wing span has also led to folding wing-tips being introduced as a solution for meeting airport gate requirements. Recent studies have suggested such a folding wing-tip solution may be incorporated with spring devices in order to provide an additional gust loads alleviation ability in flight. The current work examines the suitability of using the Doublet-Lattice Method and the Unsteady Vortex-Lattice Method for modelling the dynamic response of such a folding wing-tip device and found that the Doublet-Lattice Method tends to over-predict the achievable gust loads alleviation because it cannot fully capture the coupling between folding and the change in local angle of attack of the wing-tip. Additional analysis also found that when using the Unsteady Vortex-Lattice Method, choosing large displacement method over linear method for solving the structural response only produced minimal difference.

I. Introduction

IN recent aircraft designs, there is an increasing focus on incorporating wings of higher aspect ratios. The increased wing span aims to improve the aerodynamic lift-to-drag ratio to achieve longer range and reduced fuel consumption as explained by the classic Breguet range equation. However, increasing the wing span also increases structural weight, therefore it is a trade-off between aerodynamic gains and weight penalty. In addition, the longer wing span could lead to operating difficulties as existing airport gates may be too narrow. The latest B-777 aircraft overcomes this restriction by incorporating a mechanism to fold up its wing-tips as it taxies to the airport gate[1].

A preliminary study[2] has suggested folding wing-tips can also provide gust loads alleviation benefits, which can help towards offsetting the weight increase from the increased wing span through reduced structural requirement. The mechanism behind the gust loads alleviation property relies on the strong geometric link between the orientation of the axis of which folding of the wing-tip occurs and the effective geometric twist of the wing-tip as it folds, which is described by

$$\Delta\alpha = -\tan^{-1}(\tan\theta \sin\gamma) \tag{1}$$

where the orientation of the axis is expressed as the hinge angle γ in Figure 1 and the fold angle θ in Figure 2 respectively.

[1] Research Associate, Department of Aerospace Engineering.
[2] Research Associate, Department of Aerospace Engineering.
[3] Lecturer in Aerospace Engineering.
[4] Airbus Royal Academy of Engineering Sir George White Professor of Aerospace Engineering, AFAIAA.
[5] Flight Physics Department.

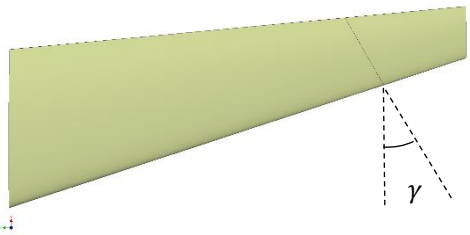

Figure 1 Hinge angle γ.

Figure 2 Fold angle θ.

A zero-angled hinge, as shown in Figure 3, thus provides no direct gust loads alleviation capability, whereas a positive hinge angle, as shown in Figure 4, can provide potential loads benefits when encountering vertical gusts due to the decreased local angle of attack of the folding wing-tip, as this action reduces the resulting bending moment contribution.

Figure 3 0° hinge angle.

Figure 4 30° hinge angle.

The aforementioned study found that using passive spring devices at the hinge can improve the gust loads alleviation performance, as it helps controlling the dynamic behavior of the wing-tip. In particular, low hinge spring stiffness and low wing-tip inertia appeared to provide the best loads alleviation performance. However, low hinge spring stiffness can cause aerodynamic deficiencies during trimmed-flight as the wing-tips can remain in a deflected position. At extremely low stiffness setting, flutter could also occur if the wing-tip inertia is not compensated accordingly through adding mass[3]. Therefore, this contrasting stiffness requirement for trimmed-flight and gust loads alleviation has led to proposed solutions such as bi-stable wing-tips[4] and active control via piezoelectric actuators[5]. Despite this complication, the folding wing-tip concept remains promising as recent research have suggested that coupling the folding wing-tip to a nonlinear spring system may provide the solution[6, 7].

This paper describes the effort in modelling folding wing-tips featuring a linear spring system at low speed. This is a follow-on work from the previous study by the authors[8], in which a folding wing-tip wind tunnel prototype of the said concept was experimentally tested. The study found discrepancies in the steady aerodynamic cases between the experimental results and predictions from the Doublet-Lattice Method (DLM)[9] in NASTRAN, which suggests a more accurate way of modelling the aerodynamics was needed. The current work investigates the suitability of the Unsteady Vortex-Lattice Method (UVLM)[10] as an alternative to the DLM. The UVLM has been considered for this work because of its ability in modelling large deformation or rotation of lifting surfaces, which is highly relevant to the dynamic response of a folding wing-tip.

II. Numerical Models

Two computational aerodynamics methods: the DLM and the UVLM are compared in this work. Since the hinge angle for the folding wing-tip devices and its effect on the loads alleviation performance is of considerable interest for this area of research, it was necessary to assess the suitability of both methods with such geometric variation. This requirement has led to constructing a numerical model for each geometric configuration individually, while keeping the number of elements in each model the same to preserve numerical consistency. Since the accuracy of the underlying Finite Element model (FEM) must be considered, especially the limitation associated with skewed cells, a decision was made to change the sweep angle of the wing while keeping the same hinge angle relative to the leading edge to ease the mesh generation process for the FEM itself. As shown in Figure 5, this arrangement still allows the effective hinge angle to be changed, but unfortunately the solution is also coupled with the effect of sweep.

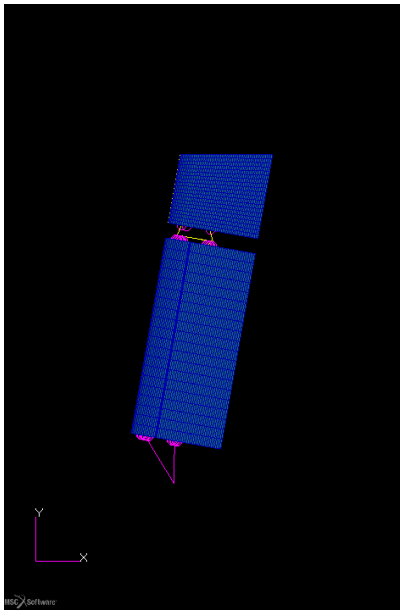

(a) Low sweep angle (10 degrees).

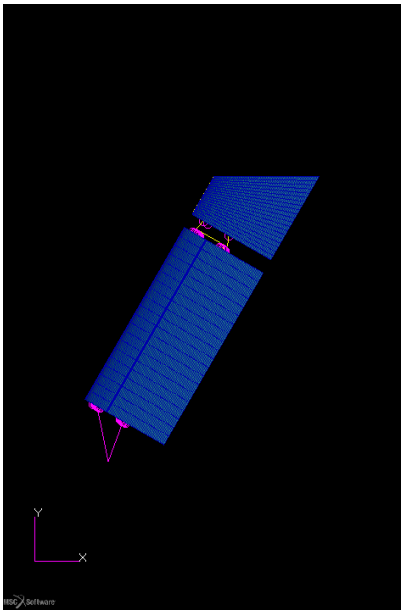

(b) High sweep angle (30 degrees).

Figure 5 Finite Element model of the folding wing-tip.

A. The Doublet-Lattice Method

The DLM is based on the integral solution of the linearized potential flow equations in the time domain. The surface is modelled by a set of elements, where each element is an acceleration-potential doublet. At each element, a velocity is calculated due to the surface motion and the external flow. The wake is modelled as an oscillating flat wake. The boundary condition is the requirement that there is no normal velocity at a control point on each panel. This leads to a linear set of equations relating the downwash induced on each panel and the pressure difference across each panel. The downwash on each panel is given by the normal velocity induced by the inclination of the surface to the flow. This means that the following system of equations can be solved for the surface pressures,

$$\boldsymbol{C_p = Aw} \tag{2}$$

where **Cp** is the pressure coefficients on the DLM panels, **A** is referred to as the Aerodynamic Influence Coefficient (AIC) matrix and **w** is the downwash vector. The forces and moments on the panel are then obtained by integrating the pressures,

$$\boldsymbol{F = SC_p} \tag{3}$$

where **F** are the forces and moments at the locations of interest and **S** is the integration matrix. Since the DLM implemented in NASTRAN was used for this work, readers are referred to the NASTRAN reference manual[11] for further details.

B. The Unsteady Vortex-Lattice Method

The UVLM solves the incompressible potential flow equations in the time domain. The surface is split up into quadrilateral elements made up of vortex line segments, forming vortex rings. At each time step, wake panels are shed from the trailing edge elements with a circulation equal to the circulation in the shedding panel. After a fixed number of times steps the wake vortex ring elements are converted to equivalent vortex particles, as shown in Figure 6. The surface elements vortex strengths can be solved for by requiring that the normal velocity through the control point on each surface panel is zero,

$$\boldsymbol{u}_{ind}^{i}.\boldsymbol{n}_i = \left(\sum_j \boldsymbol{u}_{wing}^{ij} + \sum_k \boldsymbol{u}_{wkpan}^{ki} + \sum_l \boldsymbol{u}_{wvpart}^{li} + \boldsymbol{u}_{\infty}(t) + \boldsymbol{u}_{disp} \right).\boldsymbol{n}_i = \boldsymbol{0} \tag{4}$$

where **n** is the panel normal vector and $\boldsymbol{u}_{wing}^{ij}$, $\boldsymbol{u}_{wkpan}^{ki}$, $\boldsymbol{u}_{wvpart}^{li}$ are the velocities induced by the wing panels, wake panels and wake particles respectively. The freestream velocity is given by $\boldsymbol{u}_{\infty}(t)$, which can include external disturbances such as the gust input required in a gust simulation. The relative motion of the surface due to deformation is represented by $\boldsymbol{u}_{disp}$. With the induced velocity by the wing panels expressed in terms of the unknown panel strength, Γ_j, and an influence coefficient c_{ji},

$$\boldsymbol{u}_{wing}^{ji} = \Gamma_j c_{ji} \tag{5}$$

Equation (4) can be rewritten in matrix form as

$$\boldsymbol{A\Gamma} = -\left[\boldsymbol{U}_{wkpan} + \boldsymbol{U}_{wvpart} + \boldsymbol{U}_{\infty}(t) + \boldsymbol{U}_{disp}\right].\boldsymbol{n}_i \tag{6}$$

where **A** is the matrix of influence coefficients c_{ji}.

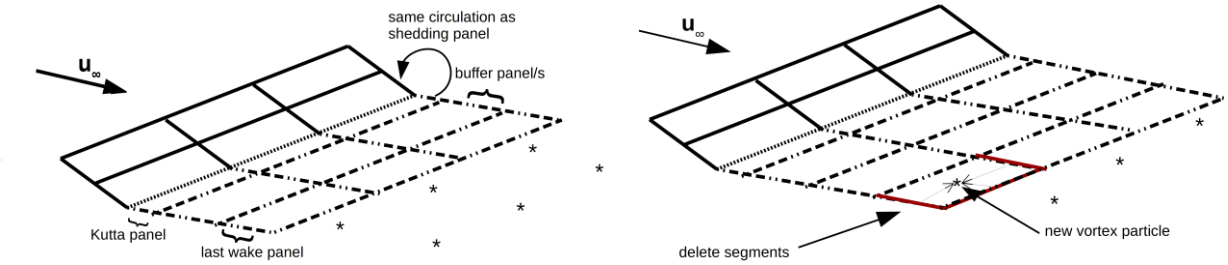

(a) Wake panels. (b) Wake panel collapse to vortex particle.

Figure 6 Wake panel arrangement of the UVLM.

1. Kutta condition

As shown in Figure 6(a), wake panels are shed from the trailing edge elements at each time step. These panels are used to enforce the Kutta condition by ensuring that the change in bound circulation on the wing is balanced by the change in circulation in the wake[12]. This is done by setting the vorticity in the first wake cell to the same as the change in vorticity over the row of panels the wake panels are being shed from, which is given by

$$\left[\frac{\partial \Gamma_{\text{span}}}{\partial t}\right]_{wing} = -\left[\frac{\partial \Gamma_{span}}{\partial t}\right]_{wake} \tag{7}$$

The trailing edge wake panel is then shed in to the wake on the next times step. After typical two times steps, the wake panels are converted to vortex particles, as shown in Figure 6(b). The vortex particles are then evolved with the local induced flow so that the force-free wake condition is satisfied.

2. Wake description

To derive the equations of for the evolution of the wake the vorticity is defined as

$$\boldsymbol{\omega} = \nabla \times \boldsymbol{u} \tag{8}$$

This vorticity evolution equation is derived from the incompressible Euler equations,

$$\frac{\partial \boldsymbol{U}}{\partial t} + \boldsymbol{U}.\nabla \boldsymbol{U} = -\frac{\nabla p}{\rho} \tag{9}$$

Taking the curl of the Euler equations leads to the resulting equations for the evolution of the vorticity,

$$\frac{\partial \boldsymbol{\omega}}{\partial t} + \boldsymbol{U}.\nabla \boldsymbol{\omega} = \boldsymbol{\omega}.\nabla \mathbf{U} \tag{10}$$

The general equation for a vortex particle α representing the vorticity contained in a volume V can be written as

$$\boldsymbol{\alpha_p}(t) = \int_{V_p} \boldsymbol{\omega_p}(\boldsymbol{x_p}, t) dV_p \tag{11}$$

The velocity induced at a point by the vortex particles is given by

$$\boldsymbol{u}(\boldsymbol{x},t)=\frac{1}{4\pi}\sum_{p}\frac{\boldsymbol{a_p}(t)\times\hat{\boldsymbol{r}}}{\|\boldsymbol{r}\|} \tag{12}$$

where $\boldsymbol{r}=\boldsymbol{x_p}-\boldsymbol{x}$ and $\hat{\boldsymbol{r}}$ is the distance unit vector. To avoid numerical problems, a vortex particle with a finite core is used[13]. The modified induced velocity is given by

$$\boldsymbol{u}(\boldsymbol{x},t)=\frac{\rho_s(\rho_s^2+5/2)}{4\pi(\rho_s^2+1)^{5/2}}\boldsymbol{a_p}(t)\times\hat{\boldsymbol{r}} \tag{13}$$

where $\rho_s=|\boldsymbol{r}|/\sigma$ and σ is the smoothing radius. In order for the wake to be force-free, the vortex particles must be moving with the local fluid velocity[14]. In the Lagrangian reference frame, the evolution of the vortex particle position is given by

$$\frac{d\boldsymbol{x}_\omega}{dt}=\boldsymbol{u}_p(\boldsymbol{x},t) \tag{14}$$

The evolution of the vortex particle strength as it travels through the domain is given by

$$\frac{D\boldsymbol{\alpha}_p(t)}{Dt}=\boldsymbol{\alpha}_p(t).\nabla\boldsymbol{u}_p(\boldsymbol{x},t) \tag{15}$$

where the last term is the gradient of the finite core particle's velocity given in equation (13). The evolution equations are solved using a forward Euler scheme, resulting in the following equation for the vortex position at discrete time (t+1),

$$\boldsymbol{x_\omega}(t+1)=\boldsymbol{x_\omega}(t)+\boldsymbol{u}(\boldsymbol{x_\omega}(t),t)\Delta t \tag{16}$$

and the updated vortex strength is then

$$\boldsymbol{\alpha}(t+1)=\boldsymbol{\alpha}(t)+\boldsymbol{\alpha}(t).\boldsymbol{\nabla u}(\boldsymbol{x_\omega}(t),t)\Delta t \tag{17}$$

3. Force calculation

The incompressible unsteady Bernoulli equations can be written as

$$\frac{\partial\phi}{\partial t}+\frac{1}{2}(\nabla\phi.\nabla\phi)+\int_{p_\infty}^{p}\frac{dp'}{p'(p')}=\frac{\partial\phi}{\partial t}+\frac{u^2}{2}+\frac{p-p_\infty}{\rho_\infty}=\frac{u_\infty^2}{2} \tag{18}$$

where ϕ is the potential field. The coefficient of pressure is defined as

$$C_p=\frac{p-p_\infty}{\frac{1}{2}\rho_\infty u_\infty^2} \tag{19}$$

Substituting the unsteady incompressible Bernoulli equation into the definition of the pressure coefficient gives

$$C_p=1-\frac{u^2}{u_\infty^2}-\frac{2}{u_\infty^2}\frac{\partial\phi}{\partial t} \tag{20}$$

The first part is the steady component and the second term is the unsteady contribution to the overall force. The differential pressure between upper and lower sides of a panel can be written as

$$\Delta p_i=\frac{|\boldsymbol{F}_i|}{S_i} \tag{21}$$

where **F** is the force acting on the panel and S is the panel area. Using equation (20) to calculate the differential pressure coefficient and using equation (21) for the steady component and relating the change in potential to the change in vortex segment strength, $\frac{\partial\phi}{\partial t}=\frac{\partial\Gamma}{\partial t}$, gives

$$\Delta C_{p_i}=\frac{2|\boldsymbol{F}_i|}{\rho_\infty S_i u_\infty^2}-\frac{2}{u_\infty^2}\frac{\partial\Gamma_i}{\partial t} \tag{22}$$

The steady force component $\mathbf{F}_i$ can be calculated from the Kutta-Joukowski theorem given by

$$\boldsymbol{F}_i=\rho\boldsymbol{u}_i\times\boldsymbol{\Gamma}_i=\rho\Gamma_i\,\boldsymbol{u}_i\times\boldsymbol{l}_i \tag{23}$$

where $\mathbf{u}_i$ is the total induced velocity on the vortex segment, Γ is the vortex strength and **l** is the vortex leg length. By combining equation (22) and equation (23), the unsteady force on a panel can be expressed as

$$\boldsymbol{F}_i' = \boldsymbol{F}_i - \rho_\infty \frac{\partial \Gamma_i}{\partial t} \boldsymbol{S}_i \tag{24}$$

4. Wake acceleration

Since the influence on a wake particle, referred to as the target particle, is calculated using all other particles in the domain, this is a problem of order O(n^2). This also means the computational cost grows rapidly, as the number of particles in the wake grows with each time step. To speed up the calculation of the wake interaction, a box tree-code[15, 16] is used. An octree is constructed by repeatedly dividing the domain into eight boxes if there are more than a set number of particles in a box. This division continues until all the particles are on the same level in the tree. With the tree defined, it is possible to partition the problem into nearfield and farfield regions. In the nearfield, the influence of particles close to the target particle is calculated directly. Outside the nearfield region, particles are agglomerated together as a single particle at a higher level in the octree. As the agglomerated particles get further away from the target particle, these too are agglomerated to the next level in the octree until the penultimate level of the octree is reached. By agglomerating the particles together, the number of particle interaction calculations needed is reduced. An example of a two-dimensional quadtree is shown in Figure 7, while Figure 8 shows the three-dimensional boxes used to calculate the influence on a point close to the wing-tip modelled in this work. For the smallest boxes, the interactions are calculated directly, while the influence for the largest boxes is calculated using a single particle agglomerated from all the particles within the box itself.

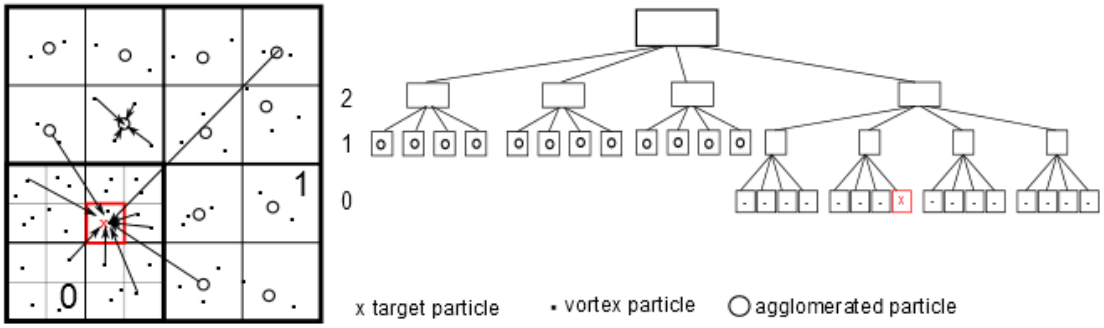

Figure 7 Example quadtree agglomeration and interaction.

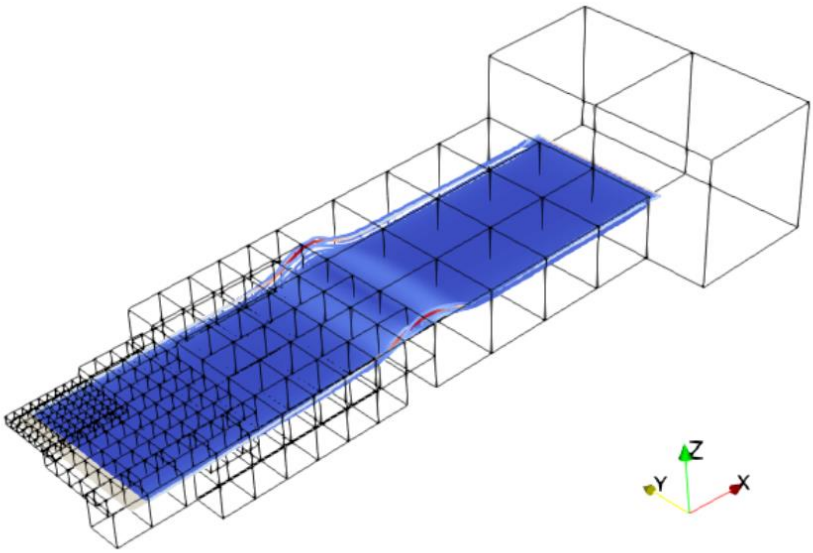

Figure 8 Octree box structure for a particle close to the wing-tip.

C. Coupling

The NASTRAN software development kit enables development of interfaces between NASTRAN and external codes such as the UVLM. The OpenFSI[17] interface allows NASTRAN to send displacements and velocities to an external code and receive back nodal forces and moments. The OpenFSI interface supports two different approaches for dynamic coupling. The first approach is explicit coupling where the codes are loosely coupled for one iteration per time step. All simulations in this paper used the second approach, which is implicit coupling where multiple iterations are carried out per time step until the load in the structure and the aerodynamics are in equilibrium, as illustrated by Figure 9. The OpenFSI coupling is run through NASTRAN SOL400 which means the analysis can be used for both linear and non-linear structures.

1. *Interpolation between the Structural and Aerodynamic grids*

The structural and aerodynamic grids typically do not coincide. Therefore, a method is needed to transfer the forces from the aerodynamic grid to the structural grid, and the displacements and velocities from the structural grid back to the aerodynamic grid. The forces on the structural grid are given by

$$\boldsymbol{f}_{str} = \boldsymbol{H}_{sa}\boldsymbol{f}_{aero}, \tag{25}$$

where $\boldsymbol{H}_{as}$ is the force splining matrix, and $\boldsymbol{f}_{str}$ and $\boldsymbol{f}_{aero}$ are the forces on the structural and aerodynamic grids respectively. The displacements in the aerodynamic grid are given by

$$\boldsymbol{u}_{aero} = \boldsymbol{H}_{as}\boldsymbol{u}_{str}, \tag{26}$$

where $\boldsymbol{H}_{sa}$ is the displacement splining matrix, and $\boldsymbol{u}_{aero}$ and $\boldsymbol{u}_{str}$ are the displacements on the aerodynamic and structural grids respectively.

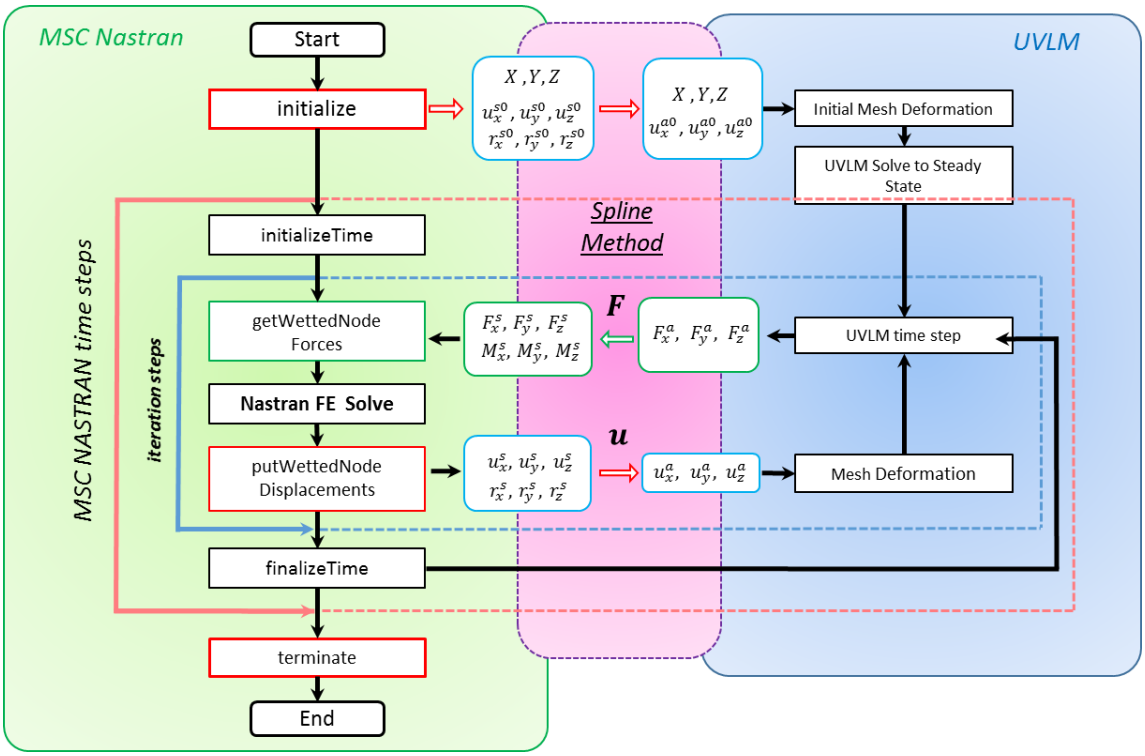

Figure 9 OpenFSI interface for coupling with UVLM.

III. Results

Both the DLM and the UVLM based models were tested over a range of hinge spring stiffness, k_θ, from 1E-7Nm/rad to 1E9Nm/rad, in sweep angle configuration of 10 degrees as well as 30 degrees. The test condition was set

to a speed of 20m/s at sea-level atmospheric condition, corresponding to the reference condition used in the related work[8].

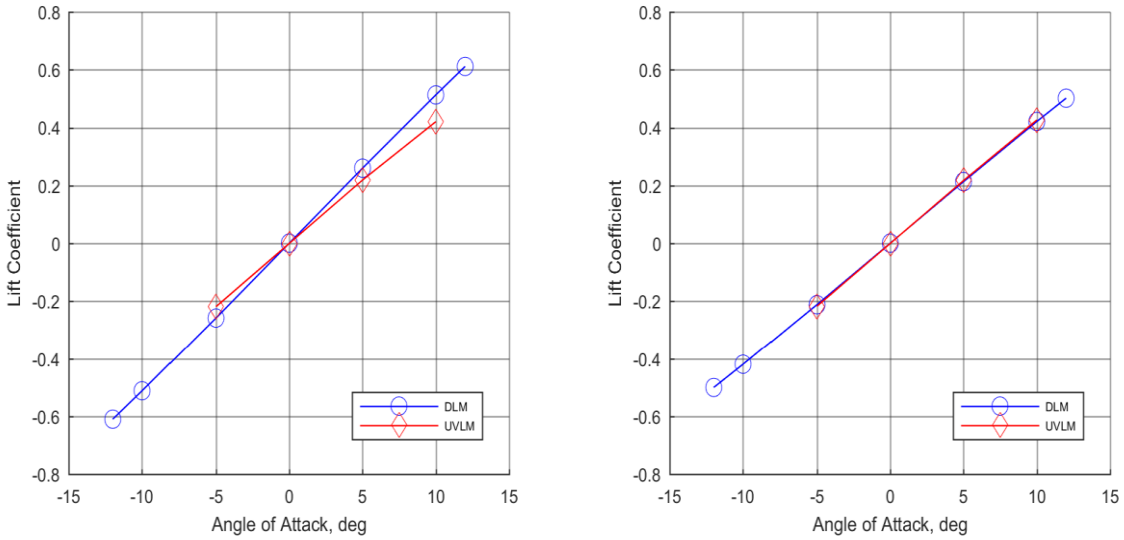

(a) Sweep angle of 10 degrees. (b) Sweep angle of 30 degrees.

Figure 10 Variation in lift against angle of attack, with k_θ = 1E9Nm/rad.

The steady aerodynamic behavior was first examined by setting the hinge spring stiffness to a high value of 1E9Nm/rad. As shown in Figure 10, the lift-curve produced by the UVLM model was shallower than the DLM prediction in the low sweep configuration of 10 degrees, but only minimal difference is observed in the case of higher sweep of 30 degrees. In Figure 11, a similar behavior can also be seen in the rolling moment. Since this high hinge spring stiffness setting is akin to a non-folding wing, these discrepancies in predicted loads may be explained by each method's sensitivity to panel discretization, as the same aerodynamic panels were used. Due to these differences, the gust loads alleviation performance may only be compared in a qualitative manner.

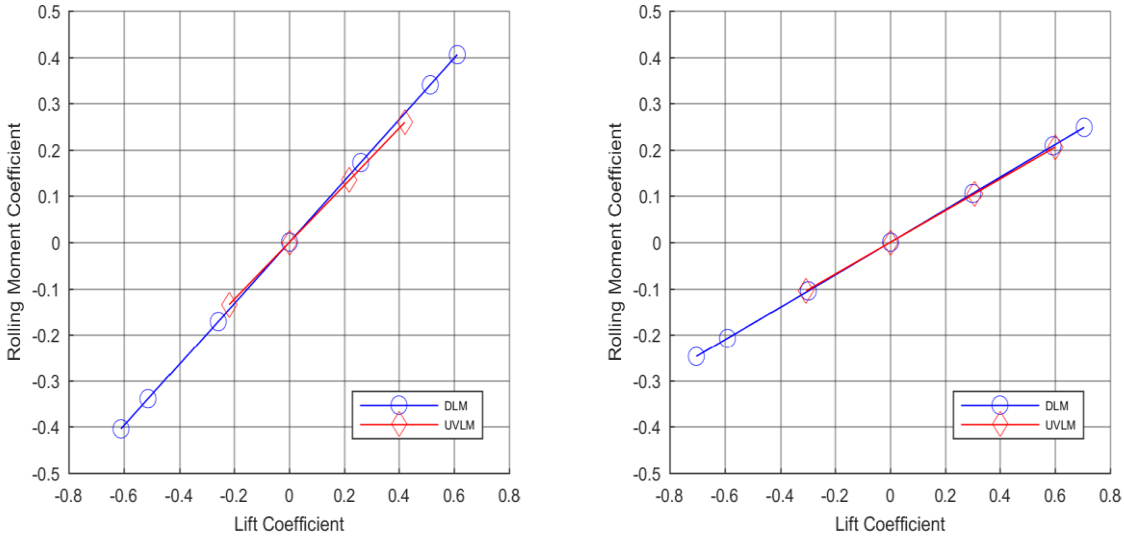

(a) Sweep angle of 10 degrees. (b) Sweep angle of 30 degrees.

Figure 11 Variation in rolling moment against lift, with k_θ = 1E9Nm/rad.

Gust analyses were conducted using a '1-cosine' gust profile of 8m in length and peak change in effective angle of attack of positive 5 degrees. In each test case, structural damping was set to the equivalent of 1% of critical damping of the first structural mode when the hinge spring is set to the highest stiffness. An additional run of the UVLM coupled to a large displacement finite element method was also carried out to investigate the impact of geometric nonlinearity has on the results.

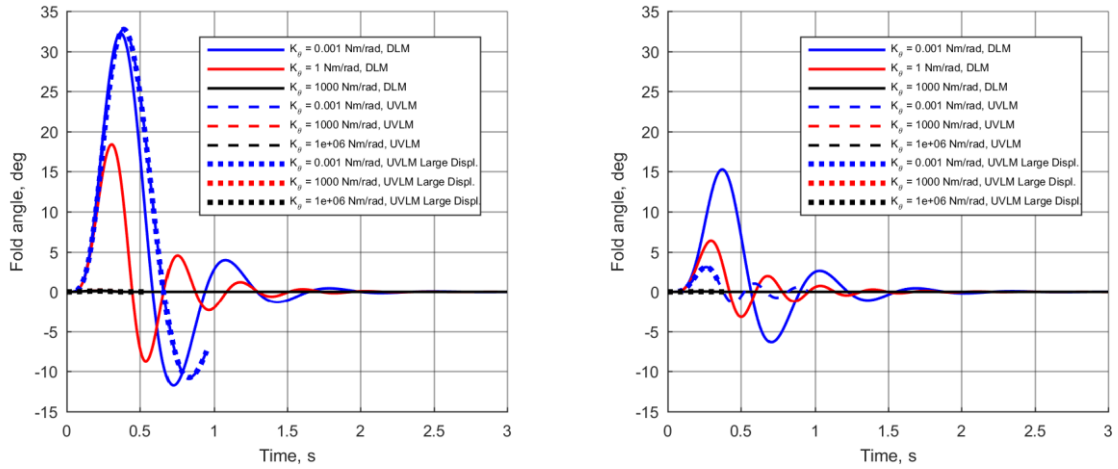

(a) Sweep angle of 10 degrees. (b) Sweep angle of 30 degrees.

Figure 12 Response in fold angle during gust encounter.

From Figure 12, the fold angle response from the DLM is more significant than the UVLM, with the large displacement UVLM runs showing minimal difference from the UVLM runs coupled to the linear method. The large fold angle response from the DLM can be attributed to the fact that the coupling between folding and change in local angle of attack of the wing-tip due to the hinge geometry is poorly replicated, meaning the reduction in angle of attack and hence the reduction in lift is not fully reflected in the results. This can be seen in the lift response from Figure 13, where the peak lift is higher from the DLM when compared with the UVLM. As shown in Figure 14, a similar trend was also observed in the rolling moment due to the same reason.

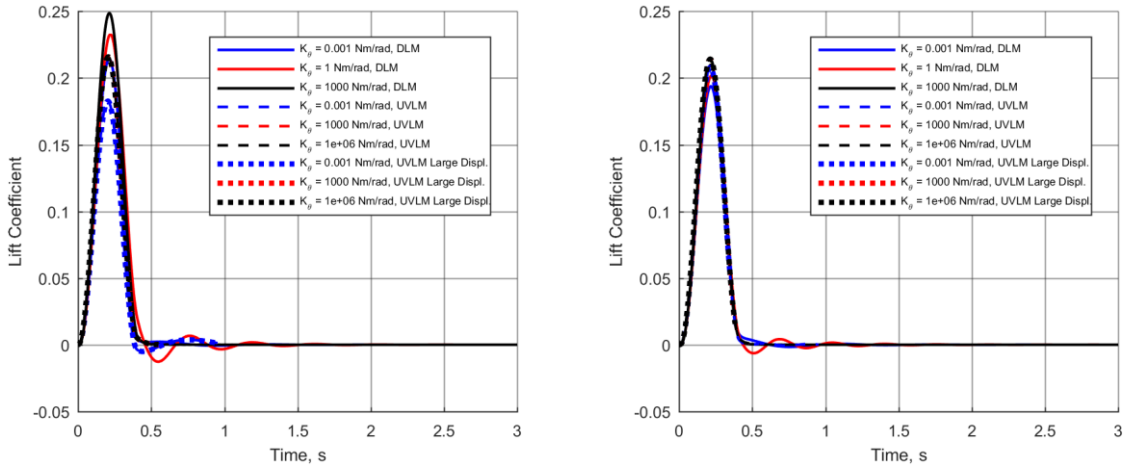

(a) Sweep angle of 10 degrees. (b) Sweep angle of 30 degrees.

Figure 13 Response in lift coefficient during gust encounter.

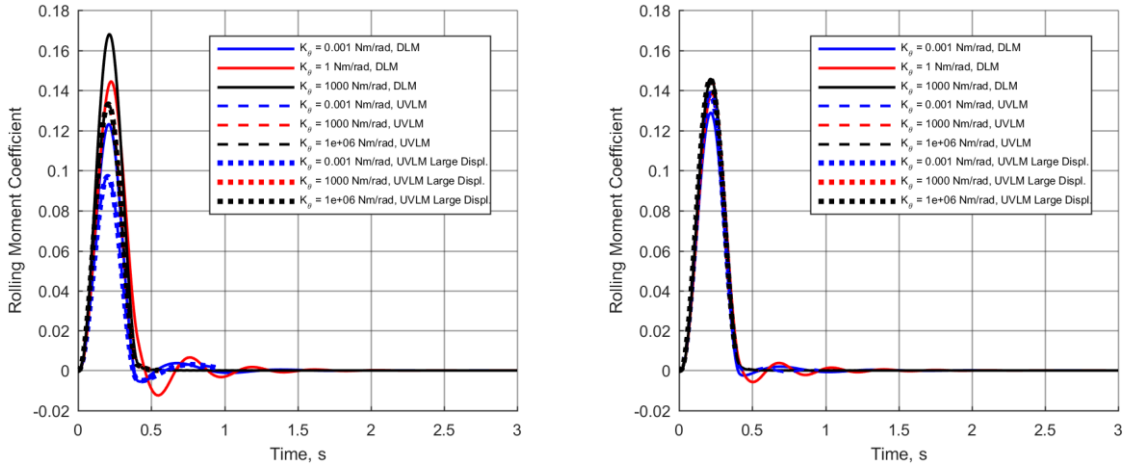

(a) Sweep angle of 10 degrees. (b) Sweep angle of 30 degrees.

Figure 14 Response in rolling moment coefficient during gust encounter.

For a larger hinge angle, the coupling between fold angle and reduction in local angle of attack of the wing-tip is stronger. Therefore, in the configuration of higher sweep angle of 30 degrees, which corresponds to a higher hinge angle, the effective aerodynamic stiffness against folding should be higher. As shown in Figure 12(b), at low hinge spring stiffness, the larger range of movement in the wing-tip from the DLM when compared with the UVLM further suggests the DLM is lacking in capturing the coupling between folding and angle of attack change, under-representing the aerodynamic stiffness of the wing-tip. For the 10-degree sweep angle configuration, the differences between the DLM and the UVLM is less significant. This is an expected observation because the coupling effect between folding and angle of attack change is less strong due to its lower hinge angle, and thus the error arising from the DLM's shortcoming is less evident.

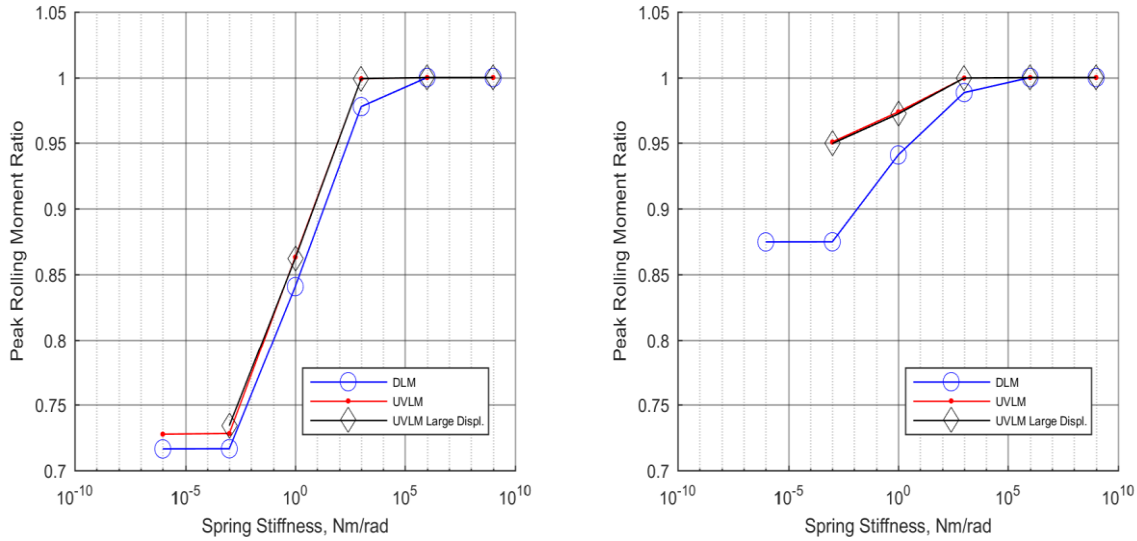

(a) Sweep angle of 10 degrees. (b) Sweep angle of 30 degrees.

Figure 15 Variation in peak rolling moment against hinge spring stiffness.

In Figure 15, the ratio of peak rolling moment for the DLM and the UVLM are shown. The values shown are normalized by the corresponding configuration with a hinge spring stiffness of the highest, therefore a lower value indicates a lower peak rolling moment or effective wing-root bending moment, and thus better gust loads alleviation performance. Both the DLM and the UVLM show good general agreement in the low sweep configuration of 10

degrees, as illustrated by Figure 15(a), showing significant gain in gust loads alleviation performance towards low hinge spring stiffness. The level of achievable gust loads alleviation was generally over-predicted by the DLM. Over-prediction was also observed in the high sweep configuration of 30 degrees as shown in Figure 15(b) and the difference is more significant towards low hinge spring stiffness. This behavior arises from the DLM's inability to fully capture the coupling between folding and local angle of attack change of the wing-tip, which underestimates the aerodynamic stiffness of the wing-tip. As explained above, lower aerodynamic stiffness leads to large folding motion, which results in a lower peak rolling moment. The difference between the DLM and the UVLM is less significant at the lower sweep configuration of 10 degrees because the corresponding the hinge angle is smaller, and thus the associated aerodynamic stiffness is also low.

IV. Conclusions

The Doublet-Lattice Method (DLM) and Unsteady Vortex-Lattice Method (UVLM) have been applied to model the behavior of a folding wing-tip concept during gust encounter. Both methods were independently coupled to NASTRAN finite element models and tested over a range of hinge spring stiffness from 1E-7Nm/rad to 1E9Nm/rad, in sweep angle configuration of 10 degrees as well as 30 degrees. The gust input for all test cases was a '1-cosine' gust of 8m in length with peak change in effective angle of attack of positive 5 degrees at forward speed of 20m/s.

Prediction of reduction in peak rolling moment produced by the DLM was found be in good agreement to that from the UVLM for the 10-degree sweep configuration, but a significant over-prediction was observed in the results from the 30-degree sweep configuration. This over-prediction behavior is evidence that the DLM cannot fully capture the coupling between folding and change in local angle of attack of the wing-tip, as the 30-degree sweep configuration corresponds to a higher hinge angle arrangement which has an inherently stronger coupling effect. Such coupling effect is key to how the folding wing-tip concept functions as a gust loads alleviation device, and thus the DLM without modification may be seen as unsuitable for modelling such concept.

Additional cases of using the UVLM coupled with large displacement finite element method have found minimal difference to using linear finite element method, suggesting the accuracy of the gust simulation for the folding wing-tip concept is more heavily dependent on capturing the motion of the aerodynamic surfaces than the structural representation.

Acknowledgments

This work is funded by the UK Aerospace Technology Institute as part of the "Wing Design Methodology" (WINDY) project. The partners in the project are Airbus Group, ARA, Future, Renishaw, University of Bristol and Cranfield University.

References

[1]Lassen M.A., D. C. R., Jones K.T. and Kenning T.B. "Wing fold controller." 2014.

[2]Castrichini, A., Siddaramaiah, V. H., Calderon, D., Cooper, J., Wilson, T., and Lemmens, Y. "Preliminary investigation of use of flexible folding wing tips for static and dynamic load alleviation," *The Aeronautical Journal* Vol. 121, No. 1235, 2017, pp. 73-94.

[3]Wilson, T., Castrichini, A., Azabal, A., Cooper, J. E., Ajaj, R., and Herring, M. "Aeroelastic Behaviour of Hinged Wing Tips," *International Forum on Aeroelasticity and Structural Dynamics*. Como, Italy, 2017.

[4]Gatto, A., Mattioni, F., and Friswell, M. "Experimental Investigation of Bistable Winglets to Enhance Aircraft Wing Lift Takeoff Capability," *Journal of Aircraft* Vol. 46, No. 2, 2009, pp. 647-655.

[5]Saravanos, D., Arrieta, A. F., Bilgen, O., Friswell, M. I., and Hagedorn, P. "Dynamic control for morphing of bi-stable composites," *Journal of Intelligent Material Systems and Structures* Vol. 24, No. 3, 2013, pp. 266-273.

[6]Castrichini, A., Hodigere Siddaramaiah, V., Calderon, D., Cooper, J. E., Wilson, T., and Lemmens, Y. "Nonlinear Folding Wing Tips for Gust Loads Alleviation," *Journal of Aircraft* Vol. 53, No. 5, 2016, pp. 1391-1399.

[7]Castrichini, A., Cooper, J. E., Wilson, T., Carrella, A., and Lemmens, Y. "Nonlinear Negative Stiffness Wingtip Spring Device for Gust Loads Alleviation," *Journal of Aircraft*, 2016, pp. 1-15.

[8]Cheung, R. C. M., Castrichini, A., Rezgui, D., Cooper, J. E., and Wilson, T. "Wind Tunnel Testing of Folding Wing-Tip Devices for Gust Loads Alleviation," *International Forum on Aeroelasticity and Structural Dynamics*. Como, Italy, 2017.

[9]Albano, E., and Rodden, W. P. "A doublet-lattice method for calculating lift distributions on oscillating surfaces in subsonic flows," *AIAA journal* Vol. 7, No. 2, 1969, pp. 279-285.

[10]Katz, J. *Low Speed Aerodynamics*: McGraw-Hill Companies, 1992.

[11]*MSC Nastran 2016 Reference Manual*: MacNeal-Schwendler Corporation, 2016.

[12]Willis, D., Peraire, J., and White, J. *A Combined pFFT - Multipole Tree Code, Unsteady Panel Method with Vortex Particle Wakes*, 2007.

[13]Winckelmans, G. S., and Leonard, A. "Contributions to Vortex Particle Methods for the Computation of Three-Dimensional Incompressible Unsteady Flows," *Journal of Computational Physics* Vol. 109, No. 2, 1993, pp. 247-273.doi: https://doi.org/10.1006/jcph.1993.1216

[14]Saffman, P. G., and Baker, G. R. "Vortex Interactions," *Annual Review of Fluid Mechanics* Vol. 11, No. 1, 1979, pp. 95-121.doi: 10.1146/annurev.fl.11.010179.000523

[15]Losasso, F., Gibou, F., and Fedkiw, R. "Simulating water and smoke with an octree data structure," *ACM Trans. Graph.* Vol. 23, No. 3, 2004, pp. 457-462.doi: 10.1145/1015706.1015745

[16]Selle, A., Rasmussen, N., and Fedkiw, R. "A vortex particle method for smoke, water and explosions," *ACM Trans. Graph.* Vol. 24, No. 3, 2005, pp. 910-914.doi: 10.1145/1073204.1073282

[17]"MSC Software Development Kit." 2014.